The Effect of Thin Film Adhesives on Mode I Interlaminar Fracture Toughness in Carbon Fiber Composites with Shape Memory Alloy Inserts

Derek J. Quade[1,2], Sadhan C. Jana[1], Gregory N. Morscher[1], Manigandan Kanaan[1]

[1] *The University of Akron*

[2] *NASA Glenn Research Center*

Abstract

Shape Memory Alloy (SMA) was placed within Polymer Matrix Composite (PMC) panels alongside film adhesives to examine bonding. Double cantilever beam (DCB) testing was performed using ASTM D5528. C-scanning was performed before testing, modal acoustic emissions (MAE) were monitored during testing, and microscopy performed post-test. Data was analyzed using modified beam theory (MBT), compliance calibration (CC) and modified compliance calibration (MCC) methods. Fracture toughness for control specimens was higher than previously reported due to fiber-bridging. Specimens with SMAs and adhesives stabilized crack propagation. Results revealed SMA-bridging; a phenomenon mimicking fiber-bridging which increased the load and fracture toughness of SMA specimens.

Keywords: Shape Memory Alloy; Polymer Matrix Composite, Fracture Toughness, Thin Film Adhesives

1. Introduction

SMA's embedded within polymer have opened a new area of interest as a hybrid actuator due to their ability to change shape. A variety of different studies have looked at shape change within constrained polymers. Characterization of nickel-titanium (NiTi) wires and NiTi strips within a variety of composites has received a fair amount of attention. Examples of this research include debonding analysis of NiTi wires within carbon fiber[1] and epoxy[2-4] systems along with thermomechanical analysis of NiTi strips in epoxy systems[4-6]. NiTi fabrication within composites has also generated research into application of SMAs in chevrons[7], stress analysis based on bending[8] and buckling[9] as well as modeling SMA debonding within a composite[10]. SMA's embedded within polymers have also opened a new area of interest based on hybrid actuators[11-13] in view of their ability to change shape on application of heat. However, SMAs and polymers are dissimilar materials, and to advance these material systems properly to other applications, further investigation is required to fully understand and to optimize the bonds between these dissimilar materials.

The ability of SMA/Polymer actuators to properly function is derived from the SMA itself. The SMA, a specific blending of various metals, is able to generate large amounts of stress when constrained through reversible, thermoelastic martensitic transitions of the crystalline structure[14]. The first blending of metals to achieve this result were nickel paired with titanium (NiTi). Austenitic crystals shift to a variety of martensitic structures during times of loading or heating. This shift is directly responsible for the

aforementioned stresses generated when constrained, as is the case when embedded within a composite[15]. The bending and flexing that occur within an SMA-PMC actuator system depend highly on the interlaminar strength between the two dissimilar materials.

Several prior investigations focused on the modeling of the actuator stresses[6,11], enhancement of the SMA-PMC bonding[1-4,10], and fabrication of an actuator system[6-8,10,12]. A majority of prior research used optically clear systems[2-12], whereby glass or aramid fibers were combined with optically clear resins. The optical clarity of the systems allowed monitoring of the strains and debonding using optical methods, such as Raman spectroscopy. Very few studies have looked at the interactions between SMAs and PMCs in systems that are not optically clear, typically involving carbon fiber reinforced polymer composites (CFRP)[1,16,17].

The goals of this research are to assess the effects of the thin film adhesives and to examine the interlaminar strength between an SMA and PMC in an actuator. A series of four 22-ply unidirectional composites panels were fabricated for the purpose. In addition to a control PMC panel with no SMA, three panels that included a central SMA sheet were manufactured. Two of the three SMA panels included additional thin film adhesives placed between the SMA sheet and the PMC adjacent PMC plies to achieve better interfacial bonding. The panels were subjected to double cantilever beam testing in accordance with ASTM D5528 method for mode I interlaminar fracture toughness of unidirectional fiber-reinforced polymer matrix composites[18]. The double cantilever beam test was chosen due to both the popularity of use within the composites community, along with the standard's ability to look at common delamination methods that occur within interlaminar composites. The addition of inner materials to a laminar composite is typically shown to increase the interlaminar failure and decrease the overall strain energy release rates of the composite system being tested[1,4-6,9-13]. Two acoustic sensors were attached to the specimens for monitoring of modal acoustic emissions (AE). AE was used for detection of debonding in the specimens during interlaminar failure. We believe this method yields better results than the visual methods of inspection of failed specimens after mechanical testing[1-4,9-11].

2. Experimental Methods

2.1. PMC Panel Layup

The PMC panel layup was based on specifications provided by ASTM Method D5528[18]. PMC panels with an average thickness of 3.56 mm were fabricated by organizing twenty-two plies with 0° unidirectional fiber orientation. This structure is schematically shown in Figure 1. Of these, eleven (11) plies of materials were put on either side of a single sheet of SMA material. A non-stick insert was placed between the SMA and the PMC (over a portion of the interface) to serve as a "pre-crack" in the DCB test specimens. Control panels were fabricated with no SMA at all, or with no adhesives, but these control panels still contained the "pre-crack" as discussed above to remain compatible with the DCB testing.

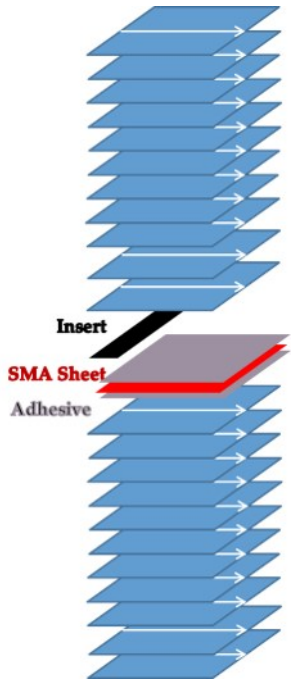

Figure 1 – Panel lay-up configuration for DCB testing: 11 plies on each side of SMA sheet bonded with thin film adhesive, non-stick insert included as pre-crack.

2.2. Materials and Fabrication

Flat annealed NiTi sheets were supplied by Johnson Matthey (San Jose, California), measuring 457 mm in length, 101.6 mm in width, and 0.127 mm in thickness. The SMA sheets were cut into rectangular specimens, 152.4 mm long and 101.6 mm wide. The SMA specimens were wiped with acetone and dried before inserting in the PMC. The PMC used was a Hex Ply 8552 Epoxy Matrix embedded with IM7 carbon fibers obtained from Hexcel (Salt Lake City, Utah)[19]. For an SMA "control" panel, no adhesive was placed between the NiTi section and the PMC. These specimens will be referred to as "SMA Control" for the duration of this study. In the remaining two panels, Hysol EA9696[20] (Bay Point, California) or Cytec FM 377U[21] (Olean, New York) thin film adhesives were used to bond the SMA sheet to the adjacent PMC plies. The pre-crack insert used in the panels was a thin polyimide film, measuring 0.0127 mm in thickness, 25.4 mm in width, and 63.5 mm in length. A mold release agent was coated onto the insert and heated to 200° C for 1 hour in order to prevent the bonding of the PMC with the insert. These panels would be processed and compared in similar fashion to the "true" control panel fabricated, which contains no adhesives or NiTi strips.

The composite specimens were assembled into panels of dimension 152.4 mm x 152.4 mm according to the lay-up guidelines presented in Figure 1. The panels were processed in an autoclave according to the recommended procedure for the Hex Ply 8552[19]. The panels were first cured for 1 hour at 110° C under full vacuum and a pressure of 0.1 MPa. The temperature was then ramped up to 176° C

and vacuum vented when the pressure increased beyond 0.2 MPa to a total pressure of 0.68 MPa for 2 hours. After curing, each panel was cut into 25.4 mm wide and 152.4 mm long specimens for conducting tests. The edges of the specimens were marked using white correction fluid to aid visual detection of crack propagation during testing. The end of the crack insert was first marked followed by markings placed at 1 millimeter increments up to 5 mm. Additional markings were placed at 5 millimeter increments up to 50 mm. Piano hinges were then attached to the pre-crack end of the specimen using an AF 163-2M thin film adhesive[22]. An image of a test specimen taken during the testing process is shown in Figure 2.

2.3. Mechanical Testing

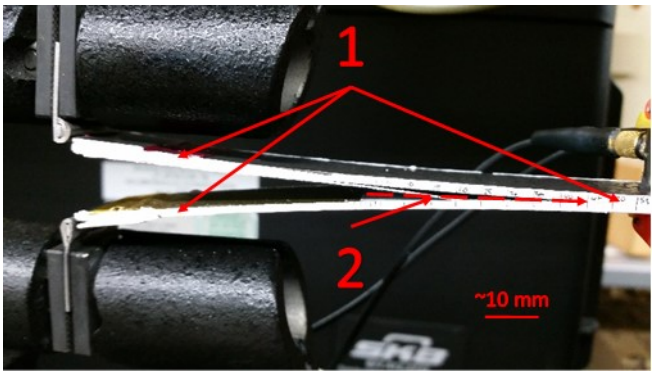

Figure 2 – DCB Specimen (1) with crack propagation (2) during test. Piano hinge placement was reversed to induce proper break

Tests were conducted on an Instron 5582 testing device running the Bluehill V 2.0 software suite. Two acoustic sensors were attached along the center line of the specimen, 12.7 mm and 25.4 mm from the end of the specimen (opposite the hinges). Vacuum grease was used to maintain contact with the specimen while the clips held the sensors to the specimen. The acoustic sensors were connected to a Digital Wave (Huntingdon Valley, PA) preamplifier, which in turn was connected to a computer running the WaveExplorer (Huntingdon Valley, PA) software suite. AE sampling rate was 10 MHz, while 2048 data points for each waveform was recorded which also included 512 data points per trigger points. Lead break tests were performed on the specimens first to make sure that the AE sensors were placed at the correct locations and were functioning properly. A double cantilever beam (DCB) setup was used for testing. The DCB tests involved pulling the sample apart at bonded hinges, with the crack propagation starting at one end.

The initial crack length (a_0) was measured from the loading hinge of the piano grip to the end of the crack-insert. A constant load rate of 5 mm/min was used for the initial loading; once the crack propagated to 3-5 mm past a_0, the specimen was unloaded back to the starting point at 25 mm/min. The specimen was then loaded again until the crack propagated to the final marks on the specimen, i.e., 50 mm from the end of the crack insert. Once the crack reached the end of the specimen, the test was stopped, and the specimen was unloaded back to the start point at 25 mm/min.

A Point Grey Research Grasshopper® 3 USB camera attached to a computer running the FlyCapture software suite was used to take pictures of the crack propagation process every 0.5 seconds. A representative image is shown in Figure 3.

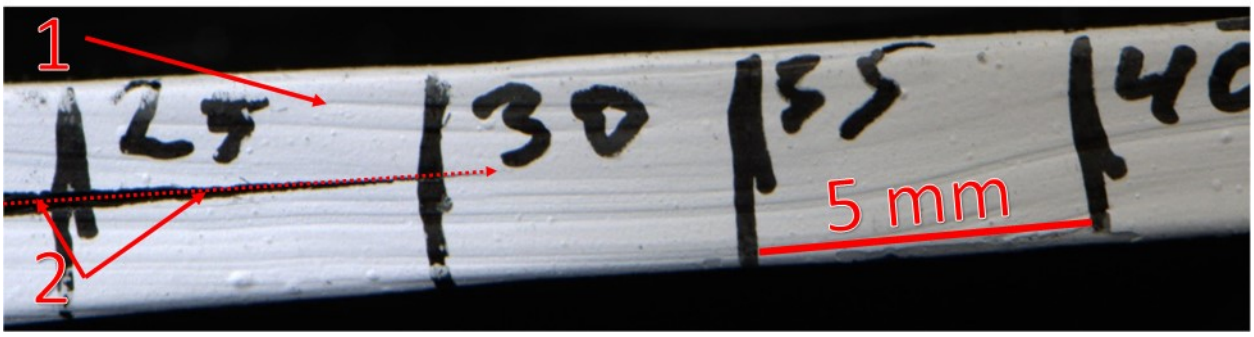

Figure 3. Side view of DCB Specimen (1) showing crack propagation (2) for specimen 1-4

As the specimens were pulled apart, acoustic events were recorded and marked at each point it occurred. Before the start of each test, pencil lead breaks (0.5 mm diameter) were performed at the edge of the samples so that the sound traveled across both sensors. The time difference of arrival between the sensors was monitored for the first peak (extensional mode). From these peaks, the speed of sound across the specimens was calculated by the distance between the two sensors (x) divided by the difference in arrival time (Δt_x).

Post-test optical microscopy was performed on an Olympus Macroscope DFC295 utilizing the Leica Applications Suite software, while scanning electron microscopy was performed on a Hitachi S-4700, both on the failed specimens.

3. Results

The analysis of data yielded information on fracture toughness. The acoustic emissive energy signals recorded at the time of experiments were added to load vs. extension graphs to facilitate data interpretation.

3.1.1. Mechanical properties

A representative set of load vs. displacement data are presented in Figure 4. These graphs are produced from the total data generated from the Bluehill software during DCB testing. Graph A represents the DCB load vs. displacement data for the control specimens (with no SMA sheet), graph B represents the DCB load vs. displacement data for the SMA control series, while graphs C and D represent the DCB load vs. displacement data for the SMA composites with FM and Hysol adhesive, respectively.

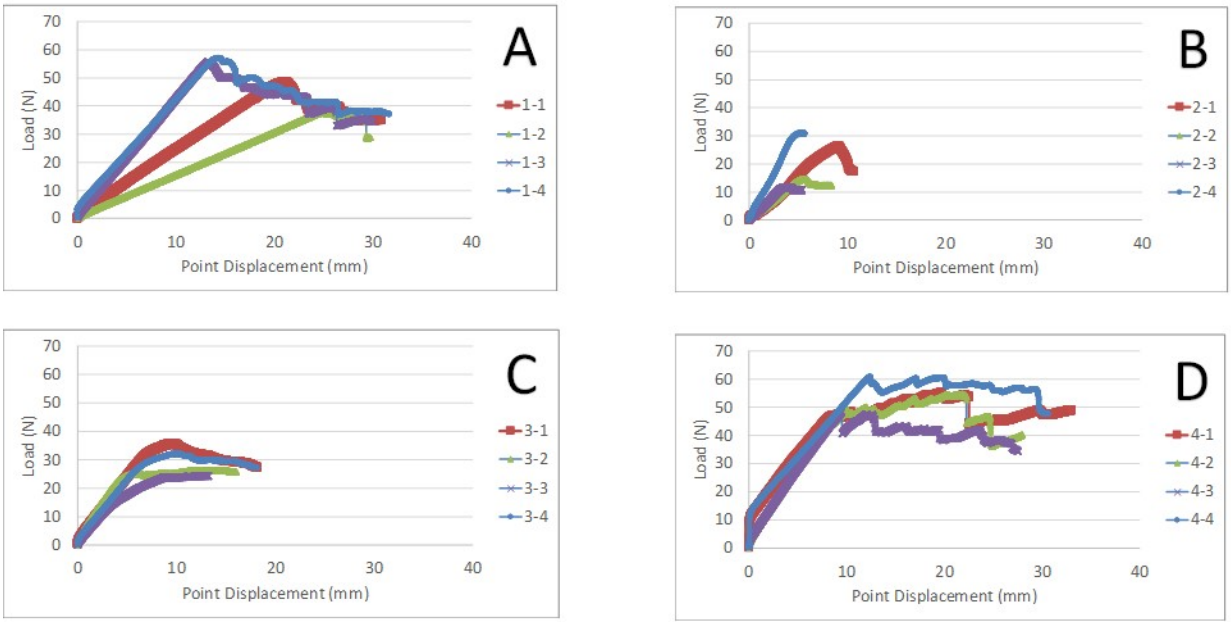

Figure 4. Load vs Displacement graphs: A - Control, B - SMA Control, C – SMA/FM Adhesive, D – SMA/Hysol Adhesive

Each graph in Figure 4 shows the four specimens used for each test group; for example, specimens 1-1, 1-2, 1-3 and 1-4 being the specimens making up control group A. Results from the control group were typical of a composite DCB test; failure was gradual and occurred after a set point of failure began propagation of the crack through the specimen. The addition of SMA for test group B led to erratic crack propagation and early failure within the specimens. The addition of FM adhesive to the SMA in image C helped regulate crack propagation, but still gave low crack growth initiation load. The addition of Hysol adhesive to the SMA in image D not only aided in stable crack propagation during testing, but gave rise to higher loads than seen in control group A.

3.2. Acoustic Emission Results

Acoustic signals generated during DCB testing were recorded by the WaveExplorer software via the acoustic sensors and preamplifier. Cumulative AE data are plotted alongside load data vs. time for each test specimen to correlate the acoustic signals originating from mechanical events. The majority of acoustic events were detected after crack growth initiation; such data are presented in Figures 5-8.

In these Figures, the red lines indicate the load of the specimen during testing, while the blue lines indicate cumulative AE signal generated during testing. For the control specimens shown in Figure 5, acoustic energy was only generated during the crack propagation phase of the DCB test. This shows that in a control situation there is a direct link between propagation of crack within the structure and acoustic energy produced.

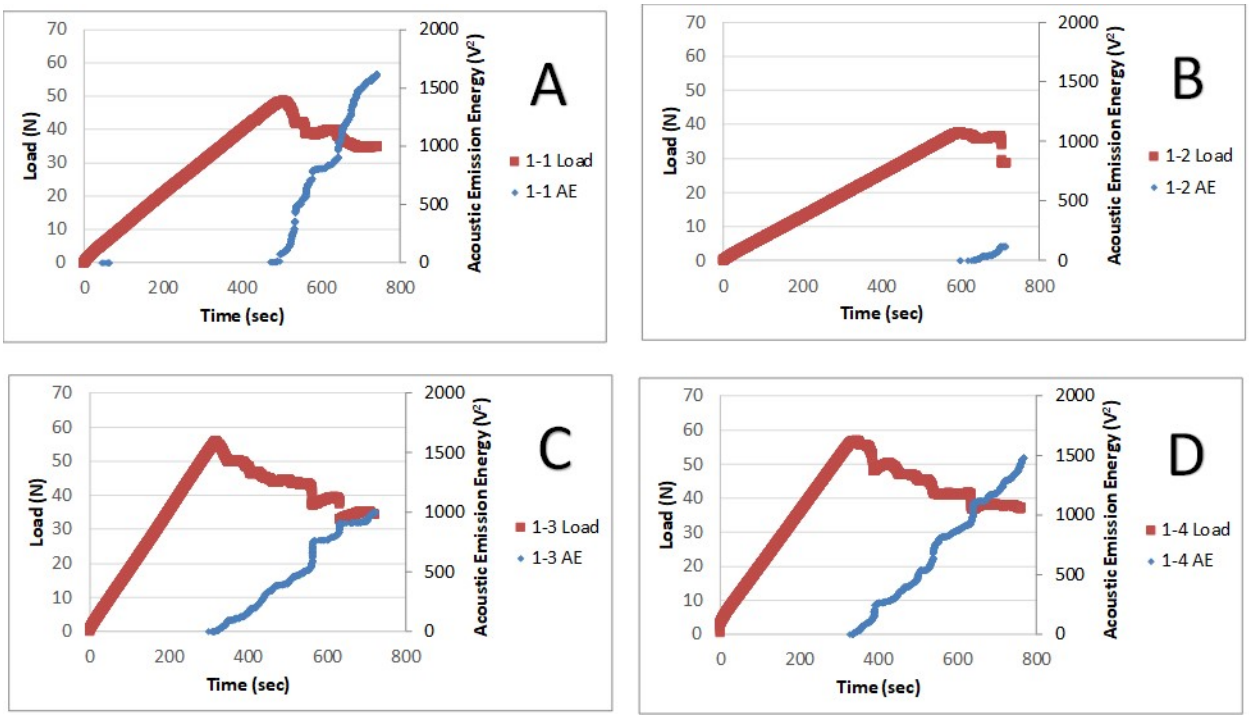

Figure 5. Load and Cumulative AE vs. Time for Control Series: A – 1-1, B – 1-2, C – 1-3, D – 1-4

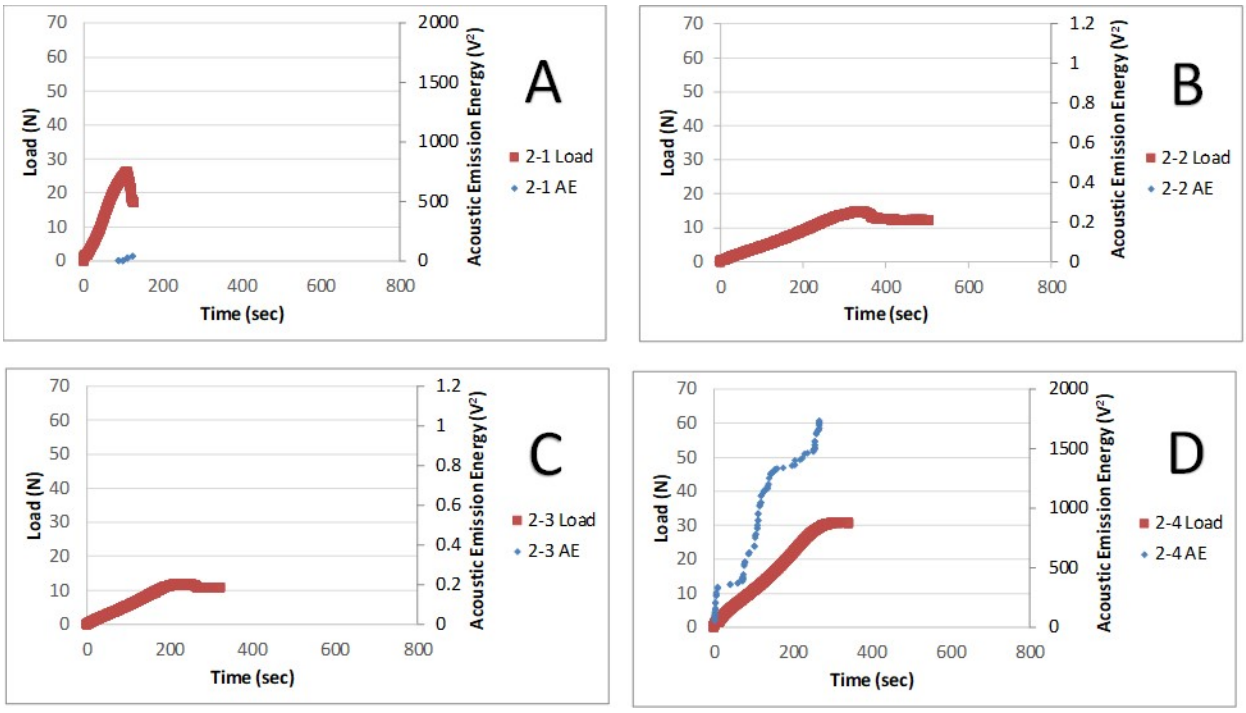

Figure 6. Load and Cumulative AE vs Time for SMA Control Series: A – 2-1, B – 2-2, C – 2-3, D – 2-4

Figure 6 shows the irregularity of acoustic data generated when a layer of SMA is introduced within the system without adhesive bonding. Acoustic signals are minimal (with the exception of specimen 2-4), indicating that low energy crack propagation occurs between the plies of PMC and SMA ply. This is a clear indication of a poor bond between the materials. If a good bond was present between the materials, the resultant "break" between bonded sections would cause more pronounced acoustic data. This is demonstrated with the introduction of FM adhesive to the specimen in Figure 7 which shows a direct increase in the load during DCB testing. However, the failure between the adhesive and PMC material generates fairly low energy acoustic signals. The same phenomenon is shown in Figure 8, where the addition of Hysol adhesive increases load capabilities during the DCB test but still gives rise to low acoustic energy signals. This phenomenon can be better explained via a peeling break compared to a fracture between the surfaces. The fracture mechanic of the SMA/adhesive interface "peeling" away from the composite will indeed produce acoustic data, but not near the range or scale of actual fractures in a control specimen (where the resin within the PMC itself is most likely failing). This effect has been shown in previous studies, and is further reinforced here via acoustic data[23-26].

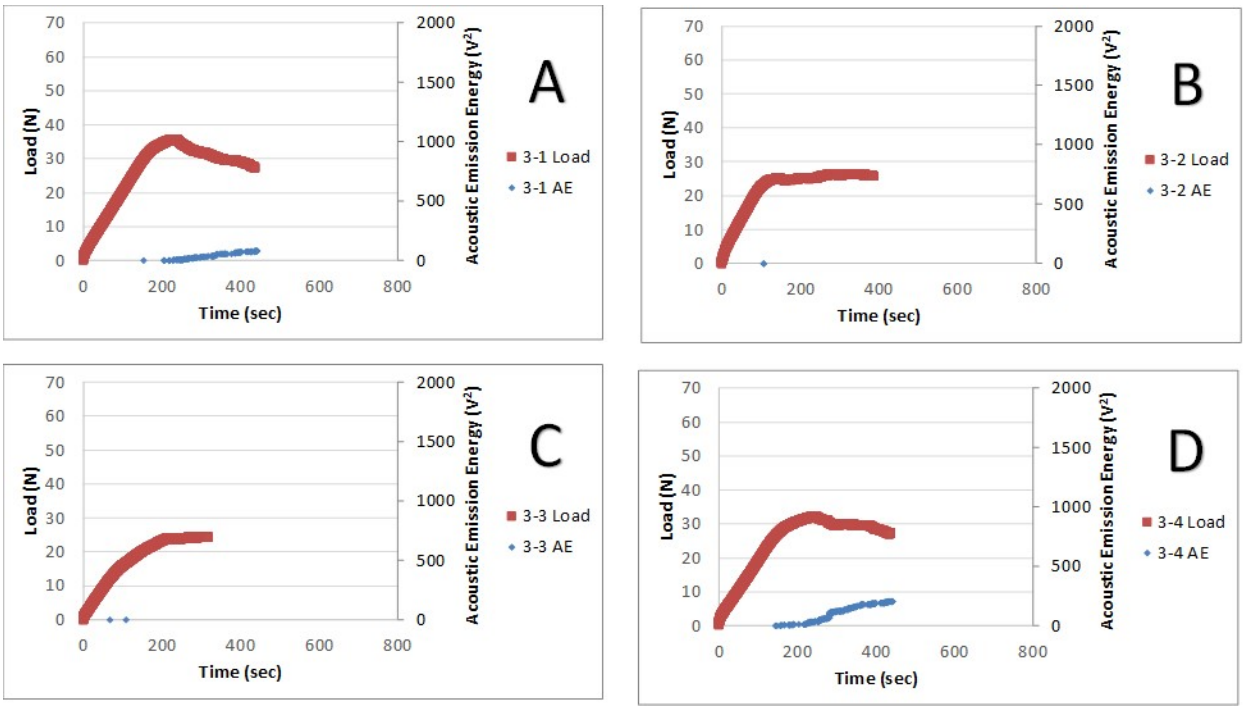

Figure 7. Load and Cumulative AE vs Time for SMA/FM Adhesive Series: A – 3-1, B – 3-2, C – 3-3, D – 3-4

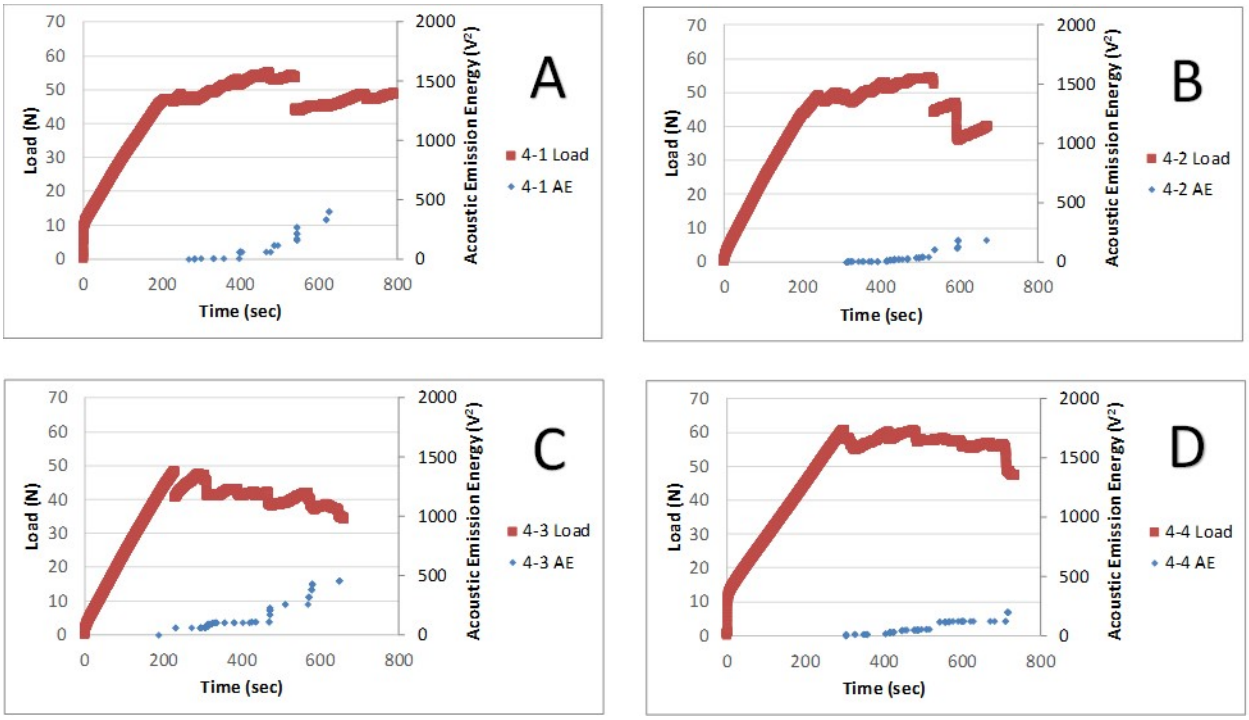

Figure 8. Load and Cumulative AE vs Time for SMA/Hysol Adhesive Series: A = 4-1, B = 4-2, C = 4-3, D = 4-4

3.3 C-scan and Microscopy Results

The effects of the SMA inserts and the adhesives on the DCB tests was evaluated by examining the images taken using C-scan, optical microscopy, and scanning electron microscopy methods. The images of the sections of the specimen interiors before and after mechanical tests were compared. These images highlighted the effect of the insert, the nature of the adhesives used, and the issues that caused irregular results in DCB testing.

3.3.1. C-scan Results

The quality of the manufactured panels was examined by C-scan as a non-destructive method of evaluating a composite by two-dimensional scanning. The results are shown in Figure 9. In these images, the dark orange or red colors from the C-scan images are indicative of a well consolidated segment. The zones with dark or lighter blue color indicate poor bonding, while white sections typically represent the voids or non-bond areas. Image A in Figure 9 shows the control panel being a well consolidated area with better overall adhesion. Image B shows that a poor bond has developed not only where the SMA has been inserted, but also between the PMC and non-stick insert itself. The addition of FM adhesive in image C improves this bond, while the addition of Hysol adhesion in image D further degrades this bond.

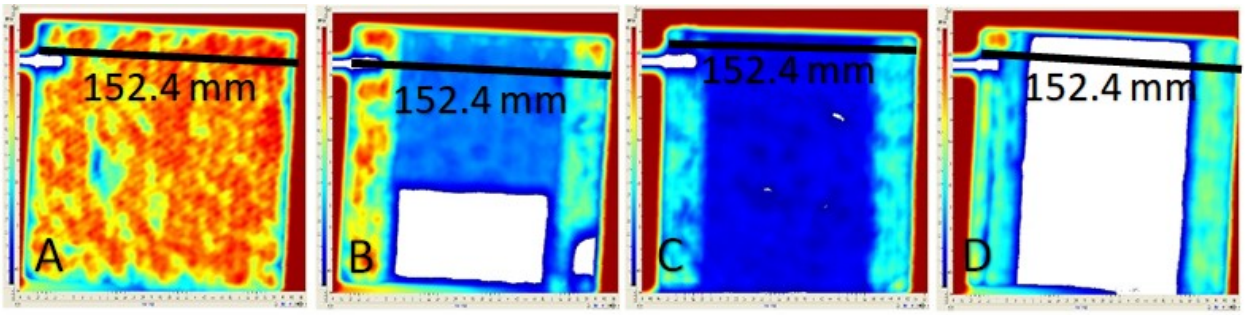

Figure 9. C-scans of DCB Panels before testing – A: Control Panel, B: SMA-Control Panel, C: SMA-FM Panel, D: SMA-Hysol Panel

3.3.2. Photography

Photographs were taken of the parts recovered after mechanical testing and before conducting optical microscopy. DCB specimens were fully separated after testing. The images in Figure 10 are the DCB sections where the SMA was no longer attached.

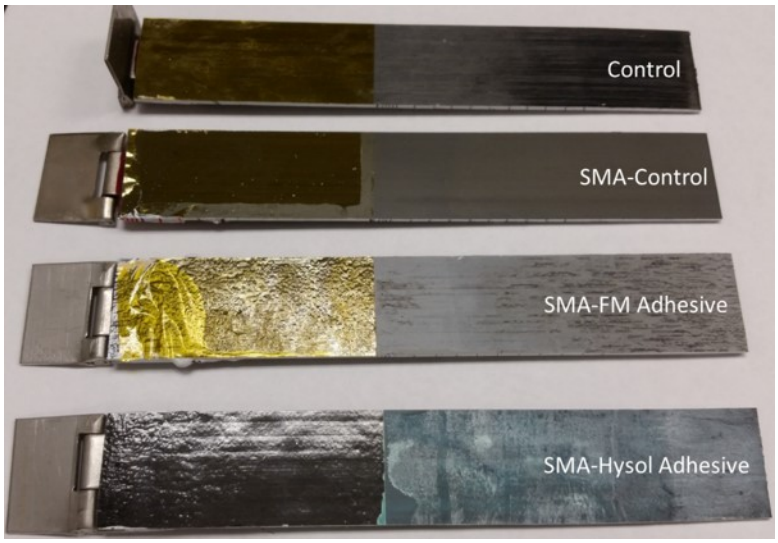

Figure 10. Post-test Images of DCB specimens

3.3.3 Optical Microscopy

The optical microscope images of specimens shown in Figure 11 highlight the end of the crack length (a=50mm).

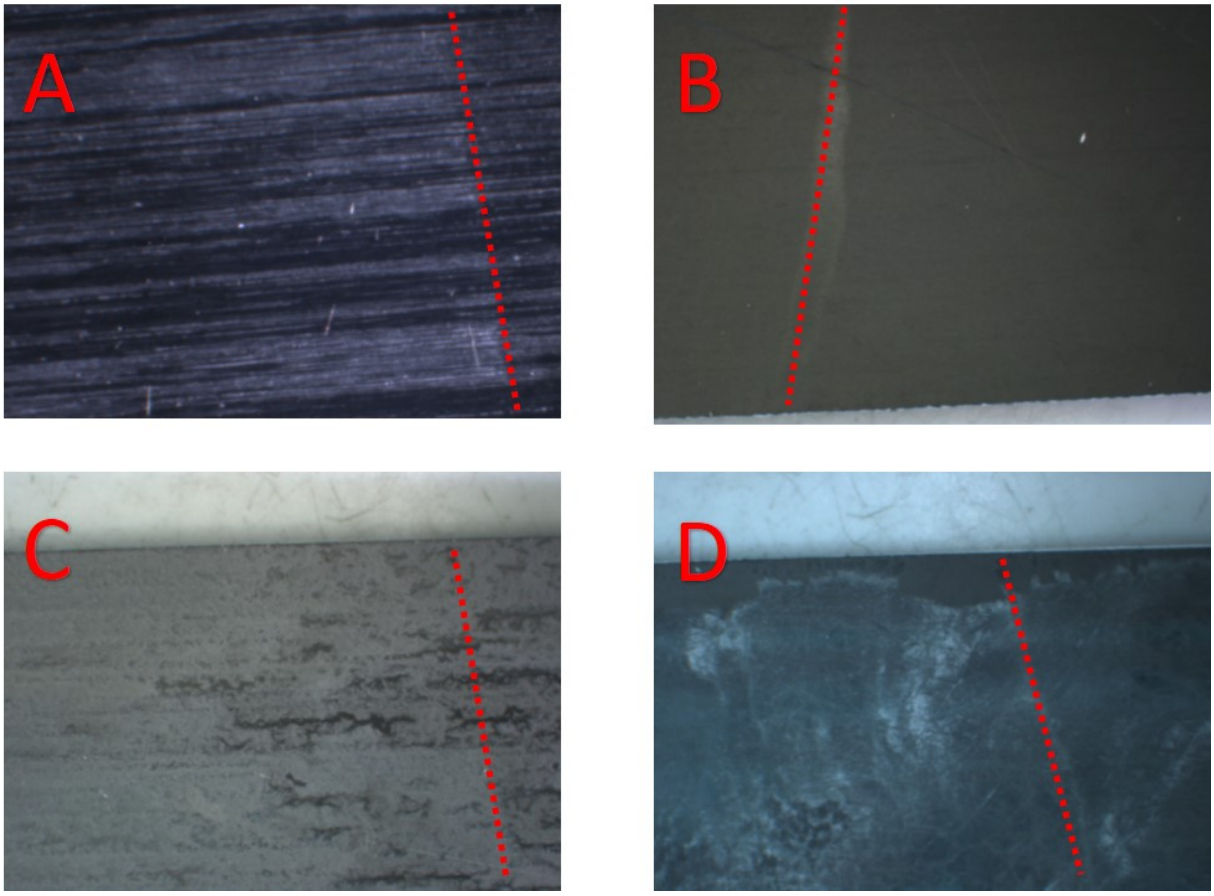

Figure 11. Crack Propagation ends of DCB Specimens: A – Control, B – SMA Control, C – SMA/FM Adhesive, D – SMA/Hysol Adhesive

Figure 12 shows optical images of SMA specimens 2-1, 3-3 and 4-2, and highlights the "bridging" effect that occurred between the SMA strip and the PMC plies during DCB testing. This is a ramification of the crack propagation phenomenon seen earlier in Figure 2; the crack traveled from one side of the PMC to the other, while the SMA "bridged" the gap between the lower and the upper halves of the specimen during DCB testing. This phenomenon was observed for all specimens that had SMA inserts.

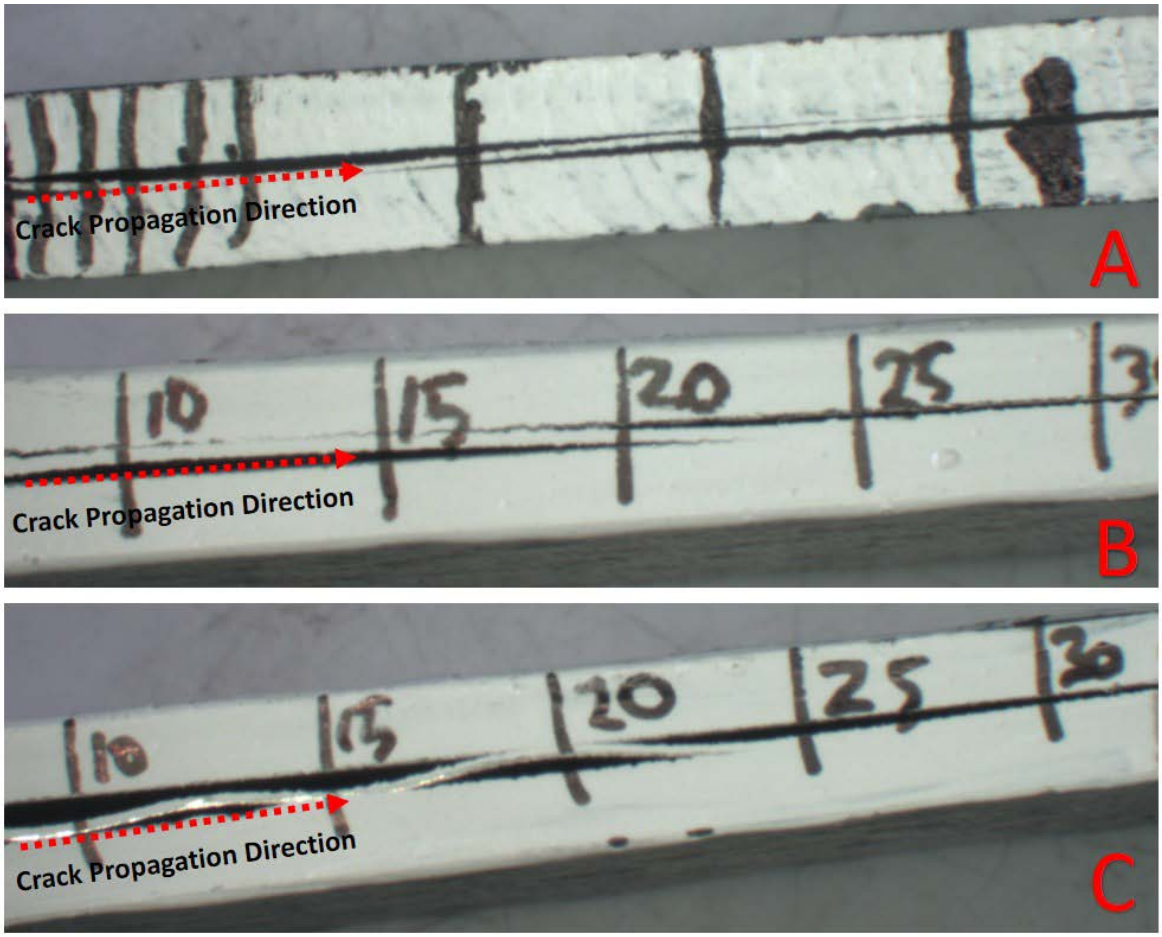

Figure 12. SMA Bridging: A – Specimen 2-1, B – Specimen 3-3, C – Specimen 4-2

3.3.4 Scanning Electron Microscopy

SEM images were taken of the area in which the pre-crack insert was placed, the area in which crack propagation occurred, and (when applicable) the bonded surface of the SMA in the area in which

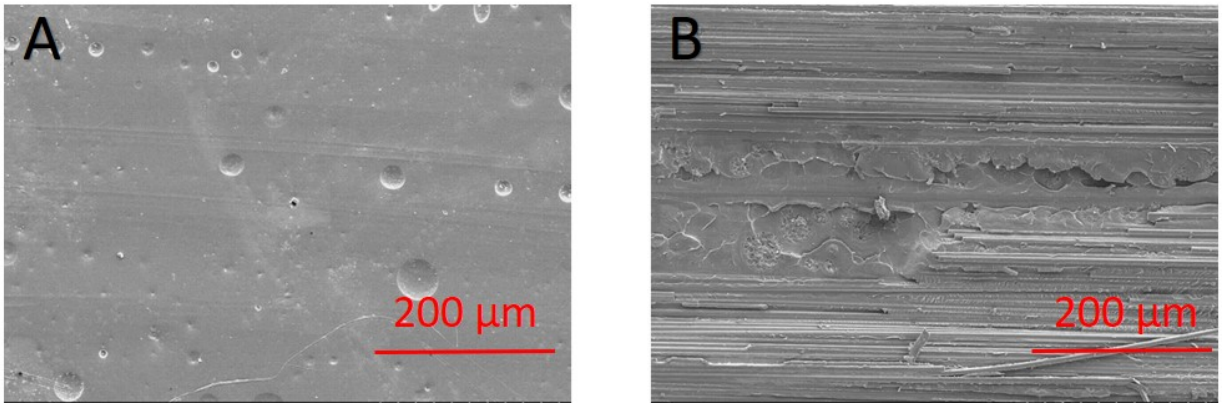

Figure 13. SEM images of the crack insert area (A) and the crack propagation area (B) of specimen 1-2

crack propagation occurred. Figure 13 shows the insert area and the crack area of specimen 1-2.

It is observed that the images in Figure 13 portray extensive bubbling in the crack insert area, while the fiber and the matrix breaks are apparent in the crack propagation area images. Figure 14 shows similar images for specimen 2-4, note in this case that the specimen contained SMA but no adhesive.

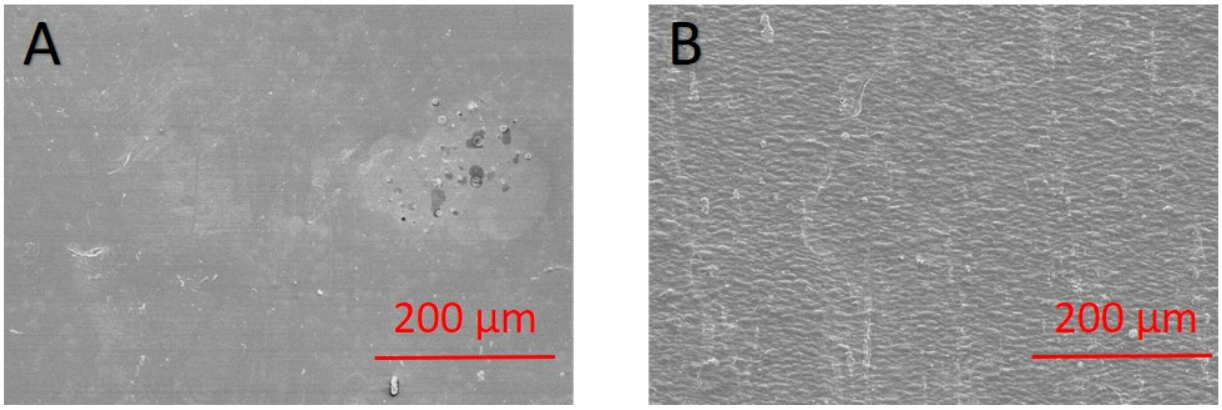

Figure 14. SEM images of the crack insert area (A) and the crack propagation area (B) of specimen 2-4

For specimen 2-4, the crack insert area was fairly smooth with no noticeable bubbles, while the crack propagation area shows little sign of fiber breaks. The texture of the specimen image is formed from processing alongside the SMA. Figure 15 shows SEM images of the PMC crack insert and crack propagation areas for specimen 3-1 which contained FM adhesive to aid bonding of the SMA strip with the PMC plies. This figure also shows the SMA surface in the crack propagation area.

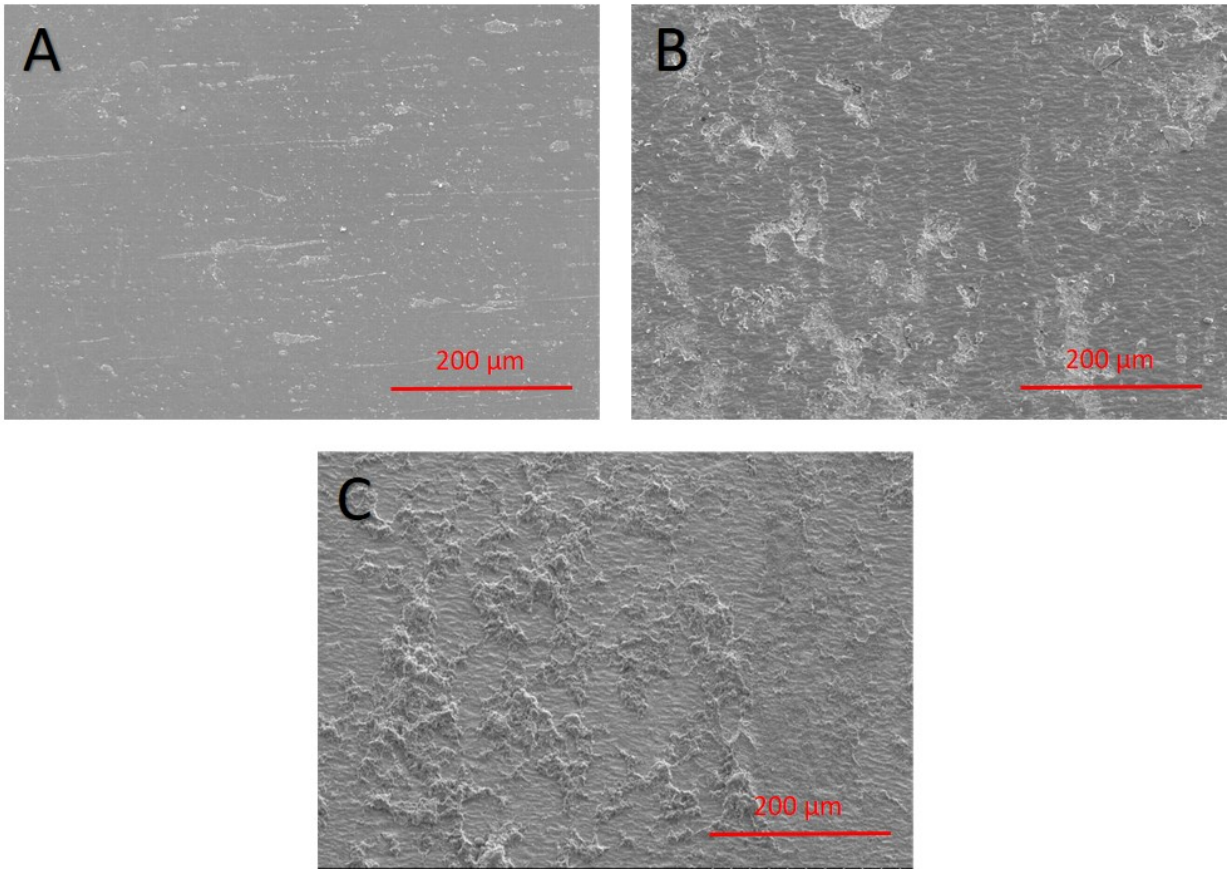

Figure 15. SEM images of specimen 3-1: the PMC crack insert area (A), PMC crack propagation area (B), and SMA crack propagation area (C)

The images in Figure 15 indicate that the FM adhesive preferentially bonded with the PMC as is apparent from the large amounts of FM residues on the PMC side of the specimen. The images of SMA show only small amounts of the FM residue. Figure 16 shows SEM images of the PMC crack insert and the crack propagation areas of specimen 4-1. In this case, Hysol adhesive was used to aid the bonding between SMA and PMC.

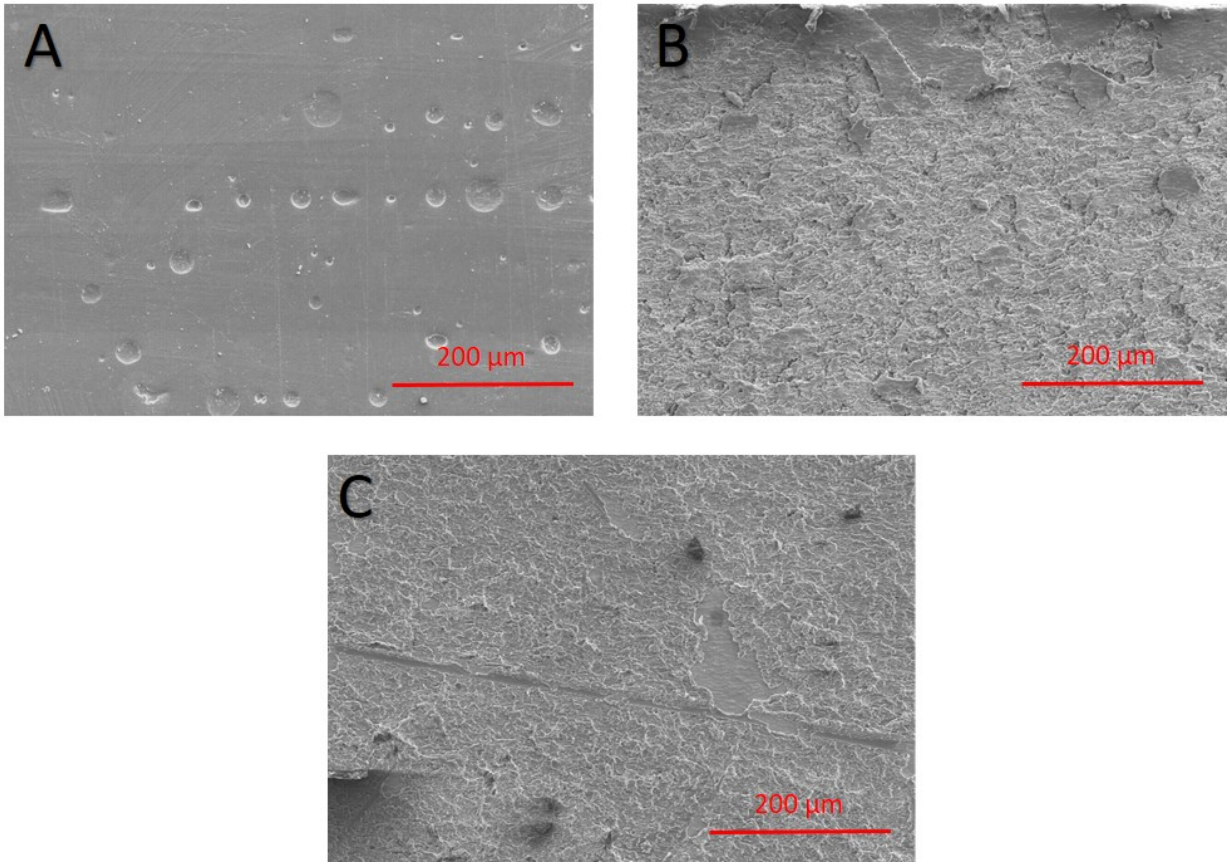

Figure 16. SEM images of specimen 4-1: the PMC crack insert area (A), PMC crack propagation area (B), and SMA crack propagation area (C)

A comparison of the images presented in Figure 16 with those of Figure 15 shows that the Hysol adhesive remnants are almost evenly distributed between the SMA strip and the PMC panel. The image in Figure 16 A indicates the presence of bubbles on the PMC crack insert area similar to those seen in Figure 13.

4. Analysis

A numerical analysis of the results from DCB testing was performed in order to highlight the differences in interlaminar toughness between the sets of specimens. This analysis utilizes the three recommended methods of calculating the mode I interlaminar toughness (G_{IC}) of the tested specimens, namely, modified beam theory, compliance calibration, and modified compliance calibration.

4.1.1. Modified Beam Theory

The DCB test data were first analyzed by correlating the delamination length with the load point displacement. The results are summarized in Figure 17. This figure shows via graph and imagery how the correlation between load/point displacement and delamination length. The red stars on the blue load line indicate when certain delamination lengths have been reached (with corresponding pictures of the delamination length).

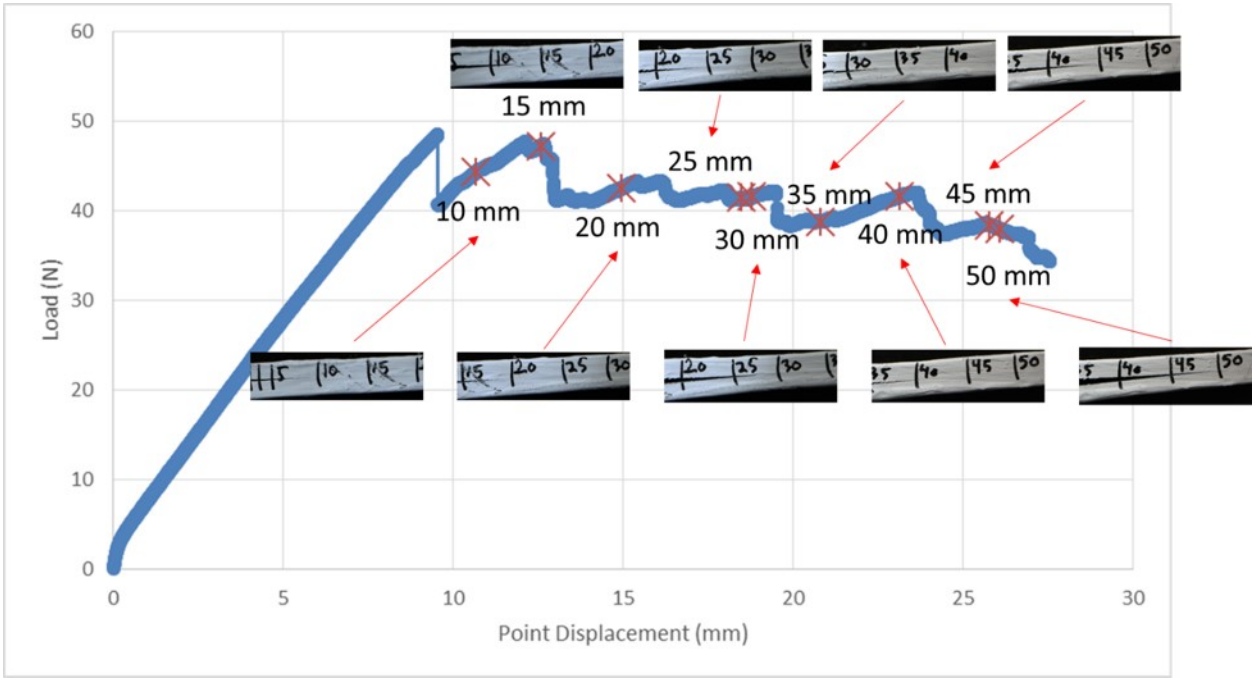

Figure 17. Correlation between crack length and separation displacement during DCB testing for specimen 4-3

The beam theory expression for the strain energy release rate of a perfectly built-in double cantilever beam is given in equation (1)[18]:

$$\mathbf{G_I = \frac{3P\delta}{2ba}} \qquad \textbf{Eq.}(1)$$

where G_I is the strain energy release rate, P is the load, δ is the load point displacement, *b* is the specimen width, and *a* is the delamination length.

This equation overestimates the value of G_I due to possible rotation that may occur at the delamination front[18]. One method used to correct for this rotation is to treat the DCB test as if there were a slightly longer delamination, $a + |\Delta|$, where Δ is calculated experimentally by the generation of a least squares plot of the cube root of compliance, $C^{1/3}$ as a function of the delamination length[18]. Compliance (C) is the ratio of the load point displacement to the applied load, δ/P. This is the essence of the modified

beam theory (MBT), which is used to calculate the Mode I interlaminar fracture toughness via equation (2):

$$\mathbf{G_{IC}} = \frac{\mathbf{3P\delta}}{\mathbf{2b(a+|\Delta|)}} \tag{2}$$

In equation (2), Δ is the least square root plot offset value. Figure 18 (a) shows schematically how the value of Δ is calculated, while Figure 18 (b) shows the actual calculation from experimental data for specimen 4-3.

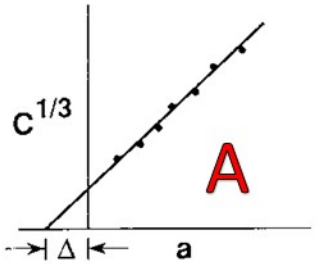

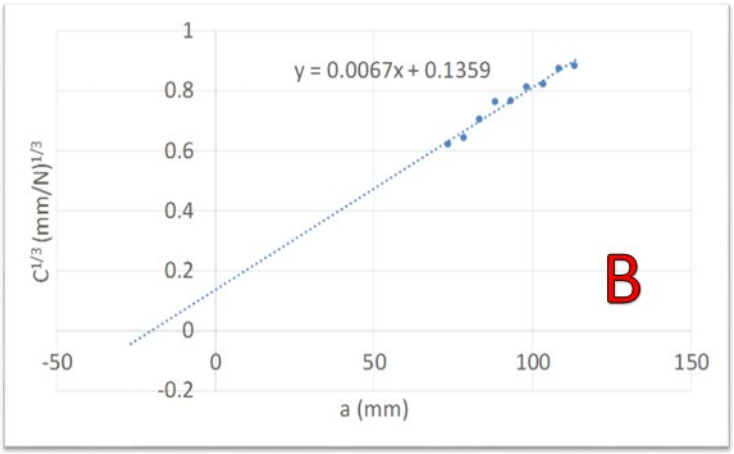

$|\Delta| = -20.284$

Figure 18. Schematic (A) and Actual (B) graphical application of the Modified Beam Theory

4.1.2. Compliance Calibration (CC)

The CC method[18] seeks to correct issues in specimen rotation via generating a least squares plot of log (δ_i/P_i) against the log(a_i) values from the visually observed delamination onset and the propagation. By fitting a least-squares line to the plotted data, the exponent *n* (slope of the line) can be determined. This value of *n* is then utilized in equation 3 to obtain the values of G_{IC}:

$$G_{IC} = \frac{nP\delta}{2ba} \tag{3}$$

In equation (3), n is the slope. Figure 19 (a) shows schematically how the n value can be obtained from a data fit, while Figure 19 (b) shows least square fit of the experimental data for specimen 4-3 to obtain the value of n=2.5062.

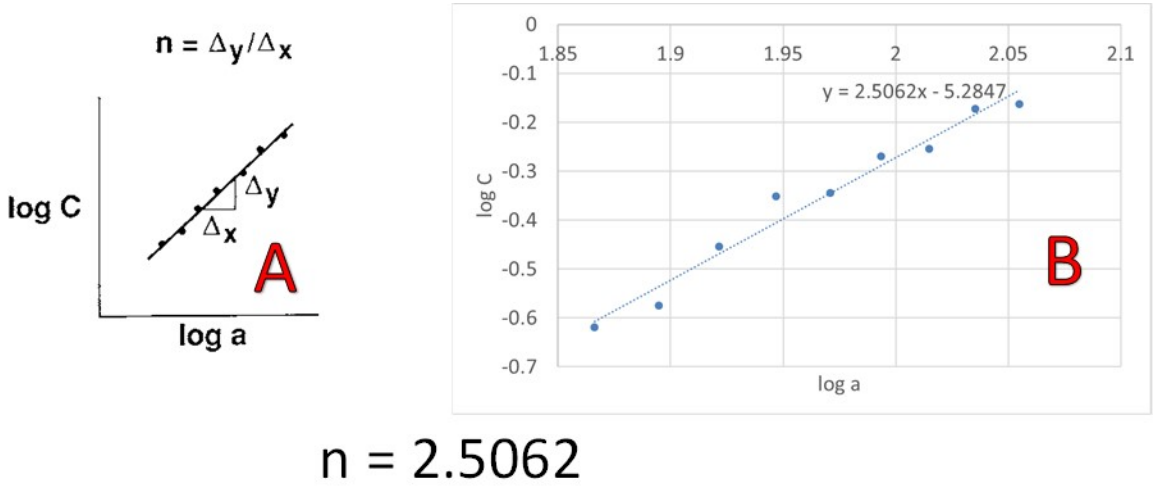

Figure 19. Schematic (A) and Actual (B) graphical application of Compliance Calibration

4.1.3 Modified Compliance Calibration (MCC)

The MCC method[18] seeks to correct issues in beam rotation and bending by utilizing a least squares plot of the delamination length normalized by the specimen thickness (a/h) against the cube root of compliance ($C^{1/3}$). This data is generated from the visually observed delamination onset values along with propagation values. From this line, a slope (A_1) is found and is used in determining the value of G_{IC} as in equation 4:

$$G_{IC} = \frac{3P^2C^{2/3}}{2A_1bh} \tag{4}$$

In equation (4), C is the compliance (δ/P), A_1 is the MCC value, and h is the specimen thickness.

Figure 20 shows a schematic of the calculation of the A_1 value (Figure 20a), along with application for specimen 4-3 (Figure 20b).

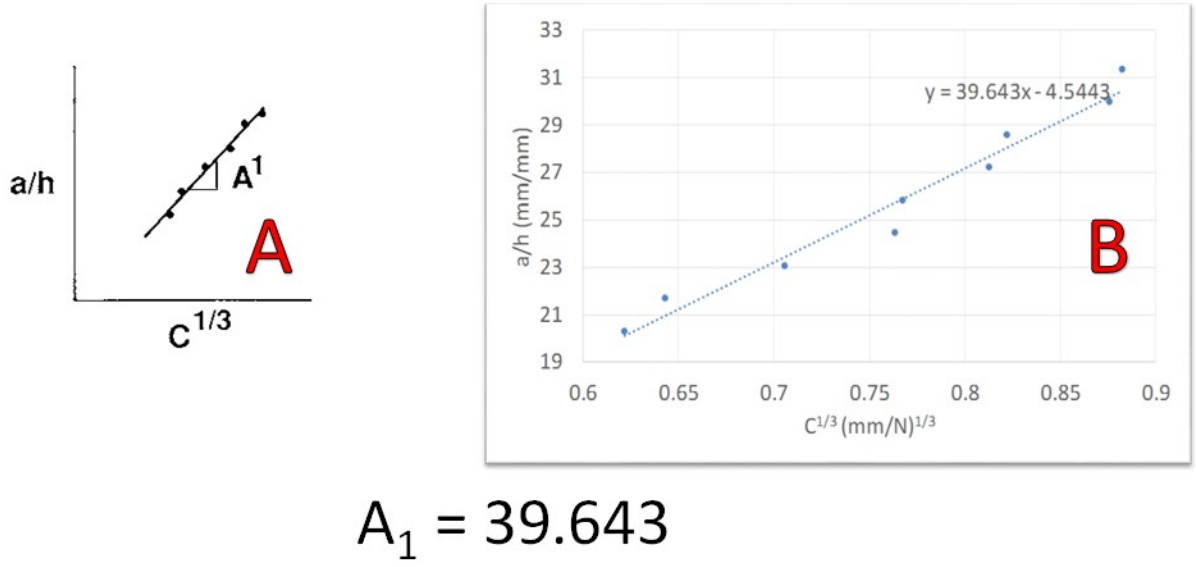

$$A_1 = 39.643$$

Figure 20. Schematic (A) and Actual (B) graphical application of Modified Compliance Calibration

4.1.4. G_{IC} Values

The G_{IC} values calculated from the use of three methods described above were plotted against the delamination length in order to obtain the delamination resistance curves of the specimens. Unfortunately, the delamination length propagation of the SMA-control specimen (Series 2) was so chaotic that calculation of reasonable G_{IC} values for this set of specimens was not possible. The crack propagation speed was sporadic in nature, and the crack progressed at significantly different rates on either side of the test specimen during delamination.

Figures 21-23 show delamination resistances curves (or R curves) for various specimen sets; the blue data points represent the MBT method, the red data points represent the CC method, and the green data points represent the MCC method.

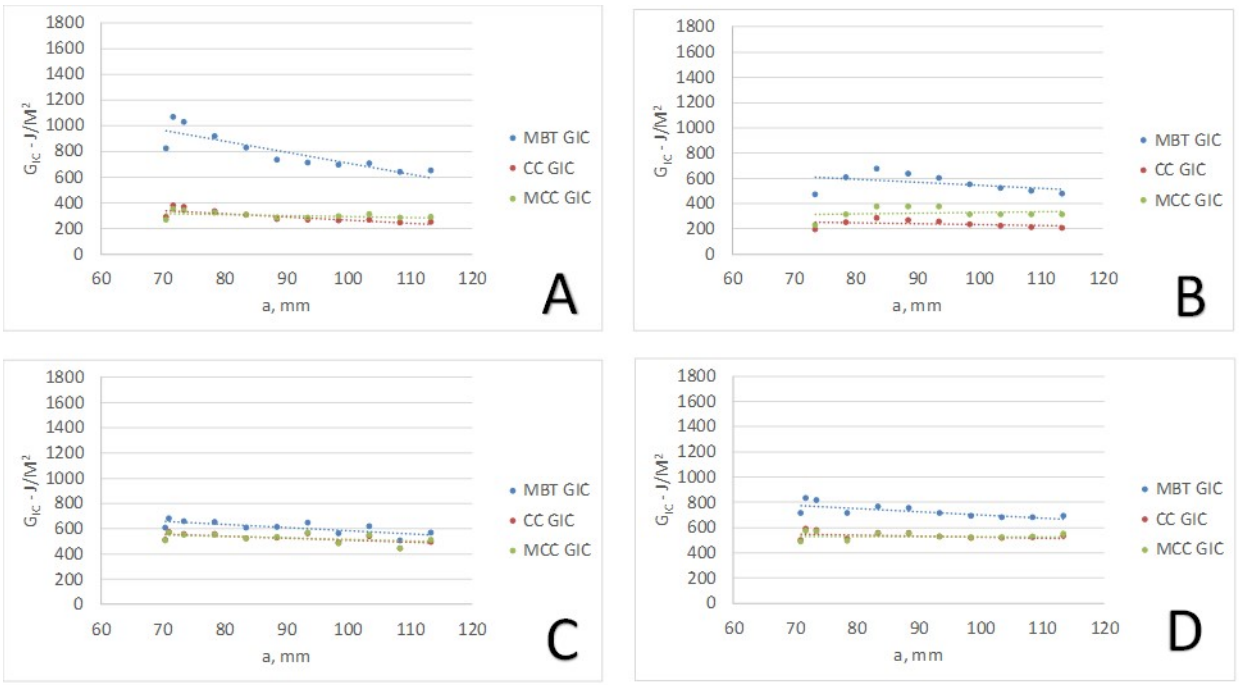

Figure 21. Delamination Resistance Curves (R Curves) for control series: A – 1-1, B – 1-2, C – 1-3, D – 1-4

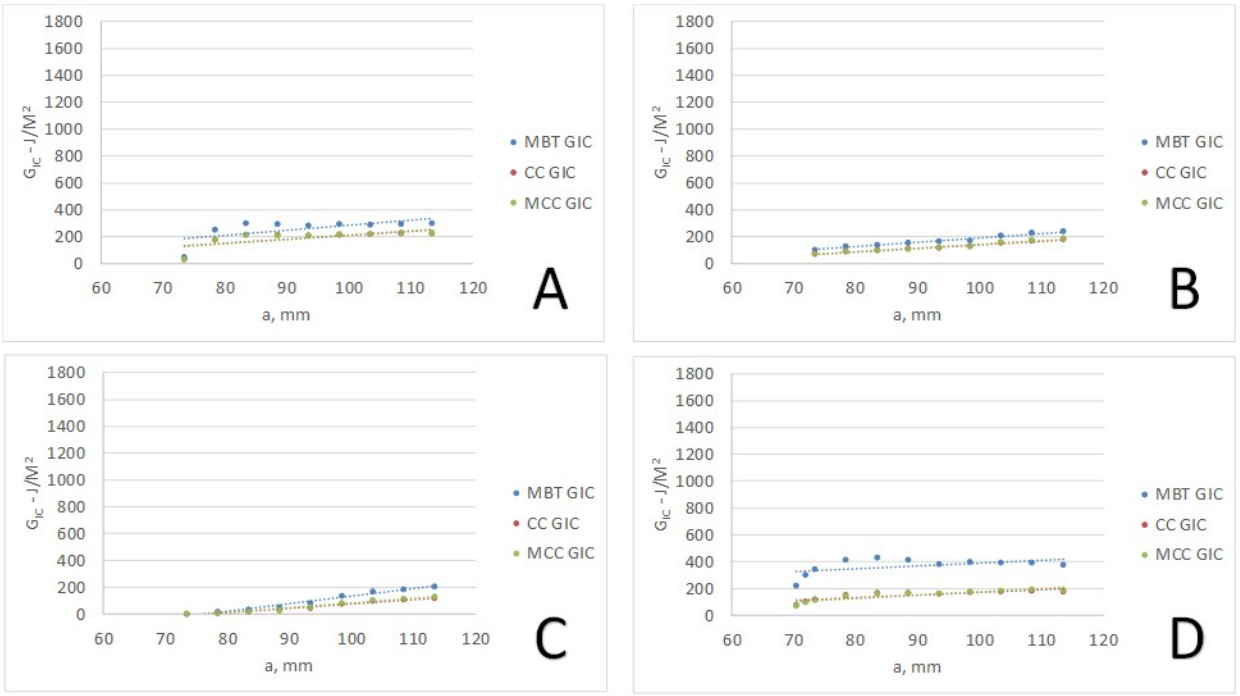

Figure 22. Delamination Resistance Curves (R Curves) for SMA-FM series: A – 3-1, B – 3-2, C – 3-3, D – 3-4

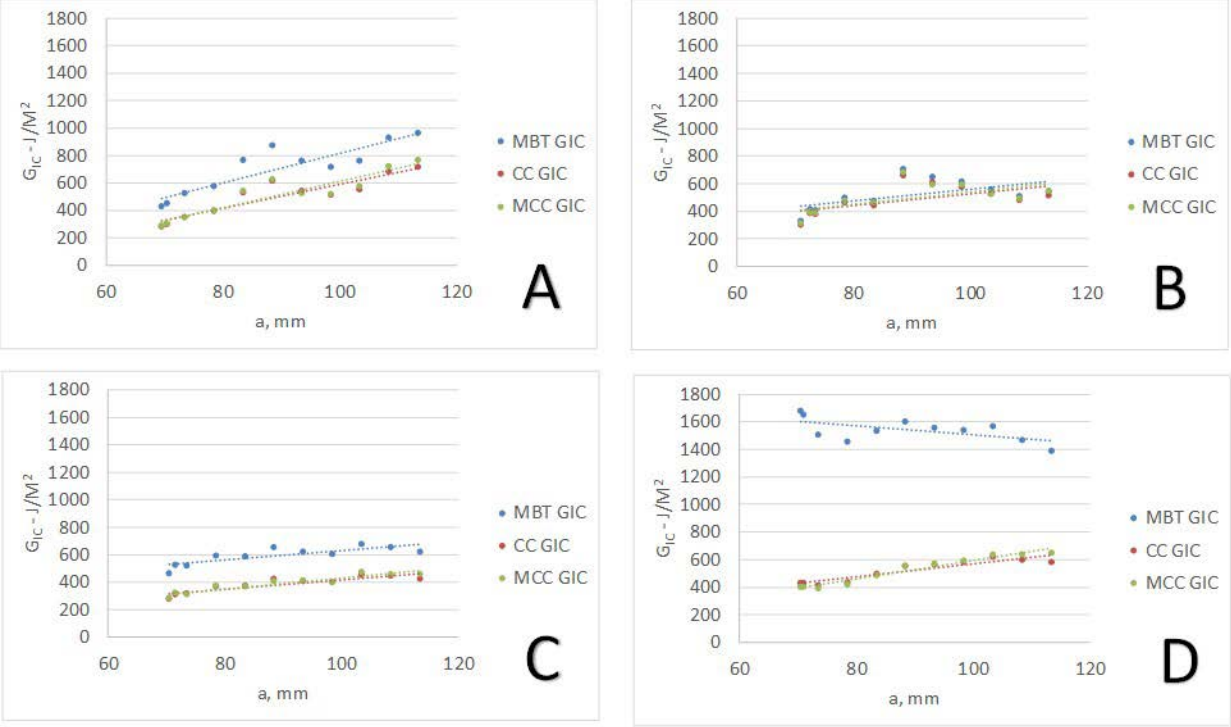

Figure 23. Delamination Resistance Curves (R Curves) for SMA-Hysol series: A – 4-1, B – 4-2, C – 4-3, D – 4-4

The R curves shown in Figure 21 are typical of a PMC composite system[28]. The line based on the modified beam theory equation in blue is typically 3-4 times higher than the compliance calibration methods[18]. Both the compliance calibration and modified compliance calibration methods are typically in agreement with each other. These results are minimized in Figure 22, where an SMA insert is bonded to the PMC via the FM adhesive. The low G_{IC} values in the R curves in Figure 23 indicate that the addition of the FM adhesive was very poor in terms of increasing the strain energy release rate of the system. The addition of Hysol adhesive, however, had opposite positive effect. Figure 23 shows that the addition of Hysol adhesive between the SMA and PMC layers increases the strain energy release rate to levels beyond those shown in the control specimen of Figure 21.

5. Discussion

The data generated in this study yielded somewhat higher numerical values compared to the data obtained using similar materials in prior work[23-26]. Prior studies reported G_{IC} values of the 8552/IM7 specimens around 0.2-0.25 KJ/m^2; the results obtained in this study fell in the range, 0.2-1.2 KJ/m^2. In addition to higher G_{IC} values, the sample sets 1 and 4 also displayed more non-linear behavior within the R curves. In comparison, typical results from DCB testing indicate a quick growth in G_{IC} values after initiation followed by a constant value[27]. The discrepancy of the reported results compared to prior studies are the outcome of both extensive fiber bridging and SMA-bridging (discussed below) that occurred during the testing.

5.1 Bridging Effect

Fiber bridging in DCB testing is a well-known phenomenon that has been shown experimentally and numerically to give G_{IC} values higher than what is otherwise observed for a specimen[18,29-33]. This is

due to fibers “bridging” the gap between the upper and lower halves of two 0° plies within a DCB specimen during the test.

In typical composite systems, the use of dissimilar ply orientations suppresses fiber bridging during a delamination failure. It is for this reason that research in this area has aimed at minimizing or eliminating this effect during the DCB test[29-33]. An increase of the toughness values can be attributed to the forces required to either break the bridging fiber between plies or to break the fiber-matrix bonds between plies (i.e., fiber pull-out). The aftermath of fiber-bridging can be seen in microscopy images of the crack propagation areas. Figure 24 gives a close-up of fiber-breaks that occurred due to bridging.

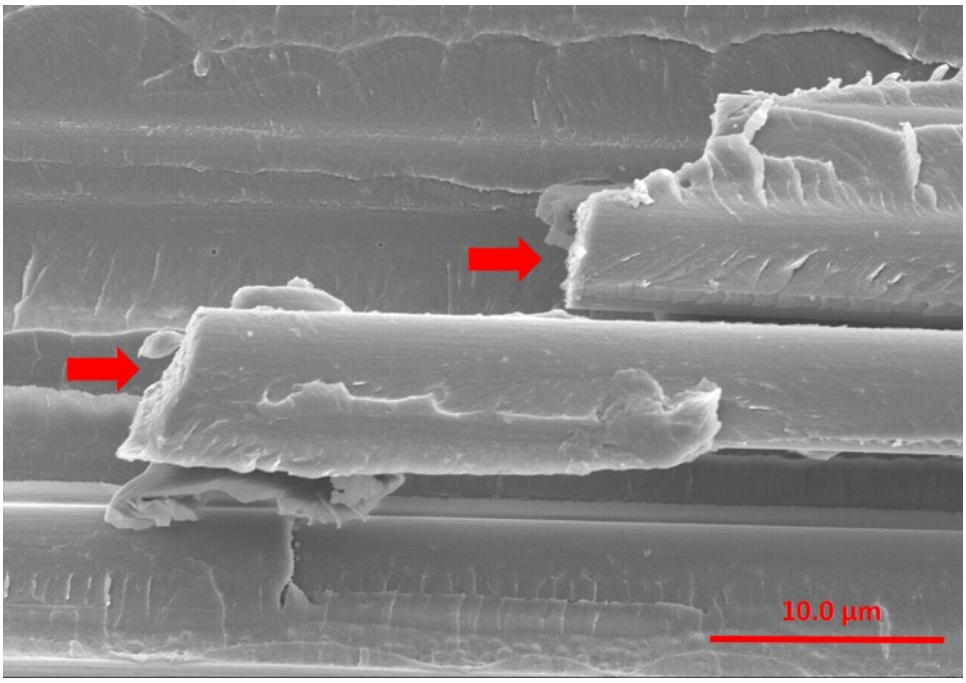

Figure 24. Fiber breaks due to bridging in specimen 1-2

Fiber bridging is indicated not only by the broken fibers, but also by the fact that the broken fibers have been debonded from the epoxy matrix within the PMC. Fiber bridging was not present in the samples with SMA; the physical barrier provided by the inclusion of the SMA eliminated this bridging effect. The inclusion of the SMA, however, lead to another type of bridging effect. This "SMA-bridging" effect was observed during testing of the specimens, and has been shown previously in Figure 12. In these images, the crack that propagates between the PMC and SMA, initiated by the polyimide crack insert, switches from one side of the SMA to the other. This phenomenon creates an SMA bridge between the upper and the lower PMC sections of the DCB specimen during the delamination process.

Similar to fiber-bridging in the control specimen, the SMA-bridging contributes to higher loads and higher calculated G_{IC} values. This is reflected in the results shown in Figure 23. The interlaminar toughness was much higher for the specimens containing Hysol adhesive in comparison to the specimens that contained FM adhesives. This was reflected in the SEM images presented in Figures 15 and 16. In Figure 15, the majority of the remnant FM adhesive was seen bonded onto the PMC panel, while in Figure 16, a somewhat even distribution of the Hysol adhesive between the PMC and SMA was observed. A stronger bond between the SMA and PMC via Hysol adhesive would also exacerbate the effect of SMA-bridging during DCB testing, thus resulting in higher interlaminar fracture toughness values. The only data that does not correlate along with better bonding for Hysol than FM was C-scan data; the images shown in Figure 9 show a qualitatively better bond within the panels joined by the FM adhesive. The inclusion of metal into the panels may negate the usefulness of the C-scan data as a reliable method for monitoring the bond strength.

5.2 Acoustic Emissions

The results from the acoustic emissions monitoring reflected the patterns that were seen in SEM images. For example, the majority of AE energy recorded from samples came from the set of control specimens, shown in Figure 5. These specimens exhibited extensive fiber-bridging during testing and thus would be expected to have higher emissive energies.

It has been shown in prior research that different AE energies are seen in composites when different failure mechanisms occur[34-37]. These can include matrix cracks, fiber breaks, and fiber-matrix debonding. These studies, while arriving at differing conclusions on the interpretation of AE results, concluded that the "loudest" AE events would occur from fiber breaks. This is due to the large amount of energy typically dissipated during this event related to the high stiffness and strength of the carbon fiber. In Figures 7-9, the AE events were either non-existent or minimal compared to the control specimens; this is likely because these AE were generated from low energy events such as matrix cracking, fiber-matrix debonding, or adhesive failure during delamination.

The bond strength difference between the two adhesives is reflected in the AE; a stronger bond (verified via SEM) between SMA and PMC was provided by the Hysol adhesive. This bonding resulted in more AE events during delamination compared to the FM adhesive bonding.

6. Conclusion

This study examined the interaction between an SMA sheet and PMC plies when subjected to double cantilever beam testing. Four different test panels were fabricated, specimens cut and subjected

to testing via ASTM standard D5528. During testing, specimens were monitored with acoustic sensors; these AE signals were then plotted against loads generated during testing. GIC results were calculated according to the three methods listed by the ASTM standard; Modified Beam Theory, Compliance Calibration, and Modified Compliance Calibration.

Without any preparation of the SMA surfaces, the addition of adhesives to the bond layer between PMC and SMA was shown to provide stable interlaminar fracture toughness results. Calculated G_{IC} values were higher than previously reported data. This inflation of interlaminar toughness values was attributed to extensive fiber-bridging within control samples along with a newly observed phenomenon of "SMA-bridging" between the SMA and PMC. In these samples, the crack traversed the SMA layer due to discrepancies in bonding between the SMA and PMC as the test progressed. Like fiber-bridging, this SMA-bridging resulted in extremely high values of interlaminar fracture toughness. Higher toughness values in the Hysol adhesive specimens were due to better bonding between SMA and PMC. Evidence of this improved bonding was seen directly in post-test SEM imaging, as well as reflected in the calculated G_{IC} values and AE levels generated during testing.

7. References

1. Araujo, CJ: Fabrication and static characterization of carbon-fiber-reinforced polymers with embedded NiTiNOL shape memory wire actuators*. Smart Materials and Structures* **2008,** *17*, 6.
2. Bollas, D: Stress Generation by shape memory alloy wires embedded in polymer composites. *Acta Materiala* **2007,** *55,* 5489-5499.
3. Parthenios, J: Adaptive composites incorporating shape memory alloy wires. *Composites: Part A* **2001**, *32*, 1735-1747.
4. Schrooten, J: Progress on Composites with Embedded Shape Memory Alloy wires*, Materials Transactions* **2002, 43,** 1-13.
5. Turner, T: Fabrication and Characterization of SMA hybrid composites*. Smart Structures and Materials* **2001,** *343,* 33-43.
6. Hisaaki, T; Elzbieta, P; Yoshihiro, E; Toshimi, S: Thermomechanical Properties of Shape-Memory Alloy and Polymer and Their Composites. *Mechanics of Advanced Materials and Structures* **2009,** *16*, 236-247.
7. Turner, T; Buehrle, R; Cano, R; Fleming, G: Modeling, fabrication, and testing of a SMA hybrid composite jet engine chevron concept. *Journal of Intelligent Material Systems and Structures* **2006,** *17,* 483-497.
8. Kim, C; Park, B-S; Goo, N-S: Shape Changes by Coupled Bending and Twisting of Shape-Memory-Alloy Embedded Composite Beams. *Smart Material Structures* **2002,** *11*, 519-526.
9. Ostachowicz, W: Dynamics and buckling of a multilayer composite plate with embedded SMA wires. *Composite Structures* **2000,** *48*, 163-167.
10. Poon, C; Zhou, L; Jin, W; Shi, S: Interfacial Debond of Shape Memory Alloy Composites. *Smart Material Structures* **2005,** *14,* 29-37.
11. Song, G; Kelly, B; Agrawal, BN; Lam, PC; Srivatsan, TS: Application of shape memory alloy wire actuator for precision position control of a composite beam*. Journal of Material Engineering Performance* **2000,** *9,* 330-333.
12. Lagoudas, DC: Modeling of a flexible beam actuated by shape memory alloy wires. *Smart Material Structures* **1997,** *6,* 265-277.
13. Hebda, DA; White, S.R.: Structural behavior of SMA composite beams. *Adaptive Material Systems* **1995,** *206*, 111-119.
14. Duering, TW; Melton, KN; Stockel, D: Engineering Aspects of Shape Memory Alloys*.* London: *Butterworth-Heinemann*, 1990.

15. J.S.N, Paine; C.A., Rogers: Review of multi-functional SMA hybrid composites materials and their applications. *Adaptive Structures and Composite Materials: Analysis and Application* **1994,** *54,* 37-45.
16. Xu, Y; Otsuka, K; Yoshida, H; Nagai, H; Oishi, R; Horikawa, H; Kishi, T: A New Method for Fabricating SMA/CFRP Smart Hybrid Composites. *Intermetallics* **2002,** *10,* 361-369.
17. Jang, BK; Kishi, T: Thermomechanical Response of TiNi Fiber-Impregnated CFRP composites. *Material Letters* **2005**, *59*, 2472-2475.
18. ASTM D5528: Standard Test Method for Mode I Interlaminar Fracture Toughness of Unidirectional Fiber-Reinforced Polymer Matrix Composites.
19. Hexply 8552; MSDS No. FTA 072e [Online]; Hexcel Composites, February 2013 https://www.hexcel.com/user_area/content_media/raw/HexPly_8552_us_DataSheet.pdf (accessed August 2018).
20. *Loctite Hysol EA 9696*; ID No. AF9118512 [Online]; Henkel Adhesives, April 2007 http://hybris.cms.henkel.com/henkel/msdspdf?matnr=698917&country=US&language=EN (accessed May 2015)
21. *Cytec FM 377U;* ID No. AEAD-00014 [Online]; Cytect Adhesives, April 2010 http://www.cytec.com/sites/default/files/datasheets/FM_377_040710.pdf (accessed May 2015)
22. *3M Scotch-Weld Structural Adhesive Film AF 163-2;* ID No. 62319253092, November 2009 http://multimedia.3m.com/mws/media/282041O/3m-scotch-weld-structural-adhesive-film-af-163-2-af-163-3.pdf (accessed May 2015)
23. Czabaj, M; Ratcliffe, J: Comparison of intralaminar and interlaminar mode I fracture toughnesses of a unidirectional IM7/8552 carbon/epoxy composite. *Composites Science and Technology* **2013,** *89*, 15-23.
24. Hansen, P; Martin, R: DCB, 4ENF and MMB Delamination Characterization of S2/8552 and IM7/8552. Technical Report N68171-98-M-5177. Hartford, UK: *Materials Engineering Research Laboratory Ltd*. (MERL); **1999**.
25. Schön, J; Nyman, T; Blom, A; Ansell, H: A numerical and experimental investigation of delamination behaviour in the DCB specimens. *Composites Science and Technology* **2000,** *60,* 173–84.
26. Murri, GB: Evaluation of delamination onset and growth characterization methods under mode I fatigue loading. *American Society for Composites* **2012,** *13,* 13-15.

27. Charentenay, F; Harry, J; Prel, Y; Benzeggagh, M: Characterizing the effect of delamination defect by Mode I delamination test*. American Society for Testing and Materials* **1984**, *283*, 84-103.
28. O'Brien, T; Martin, R: Round Robin Testing for Mode I Interlaminar Fracture Toughness of Composite Materials*. Journal of Composites Technology and Research* **1993,** *15*, 269-281.
29. Johnson, W.S.; Mangalgiri, P.D.: Investigation of Fiber Bridging in Double Cantilever Beam Specimens*. Composites Technology and Research* **1987,** *9*, 10-13.
30. Tamuzs, V; Tarasovs, S; Vilks, U: Progressive delamination and fiber bridging modeling in double cantilever beam composite specimens. *Engineering Fracture Mechanics* **2001,** *68*, 513-525.
31. Zok, Fw; Hom, CL; Large scale bridging in brittle matrix composites. *Acta Metallurgica et Materialia* **1990,** *38,* 895-904.
32. Spearing, SM; Evans, G; The role of fiber bridging in the delamination resistance of fiber-reinforced composites. *Acta Metallurgica et Materialia* **1992**, *40,* 2191-2199
33. Daridon, L; Cochelin, B; Potier, M: Delamination and fiber bridging modeling in composite samples. *Journal of Composite Materials* **1997,** *31,* 874-888.
34. De Groot, PJ; Winjem, PAM; Janssen, RBF: Real-time frequency determination of acoustic emission for different fracture mechanisms in carbon/epoxy composites*. Composites Science and Technology* **1995,** *55*, 405-412.
35. Gutkin, R; Green, CJ; Vangrattanachai, S; Pinho, ST; Robinson, P; Curtis, PT: On acoustic emission for failure investigation in CFRP: pattern recognition and peak frequency analyses. *Mechanical Systems and Signal Processing* **2011,** *25,* 1393–1407.
36. Arumugam, V; Sajith, S; Stanley, A.J: Acoustic emission characterization of failure modes in GFRP laminates under Mode I delamination. *Journal of Nondestructive Evaluation* **2011,** *30,* 213-219.
37. Ramirez-Jimenez, C; Papadakis, N; Reynolds, N; Gan, T; Purnell, P; Pharaoh, M: Identification of failure modes in glass/polypropylene composites by means of the primary frequency content of the acoustic emission event. *Composites Science and Technology* **2004,** *64,* 1819-1827